Enhancing the Thermoelectric Power Factor of $Sr_{0.9}Nd_{0.1}TiO_3$ through Control of the Nanostructure and Microstructure

D. Ekren[1], A. Golinia[1], F. Azough[1], S. J. Day[2],

D. Hernandez. Maldonado[2], D.M. Kepaptsoglou[2], Q. M. Ramasse[2], R. Freer[1]

[1] School of Materials, University of Manchester, Manchester M13 9PL, UK.

[2] Diamond Light Source, Harwell Science and Innovation Campus, Oxfordshire, OX11 0DE, UK

[3] SuperSTEM Laboratory, STFC Daresbury Campus, Daresbury WA4 4AD, U.K.

Abstract

Donor-doped $SrTiO_3$ ceramics are very promising n-type oxide thermoelectrics. We show that significant improvements in the thermoelectric Power Factor can be achieved by control of the nanostructure and microstructure. Using additions of B_2O_3 and ZrO_2, high density, high quality $Sr_{0.9}Nd_{0.1}TiO_3$ ceramics were synthesised by the mixed oxide route; samples were heat treated in a single step under reducing atmospheres at 1673 K. Synchrotron and electron diffraction studies revealed an I4/mcm tetragonal symmetry for all specimens. Microstructure development depended on the ZrO_2 content; low level additions of ZrO_2 (up to 0.3 wt%) led to a uniform grain size with transformation-induced sub-grain boundaries. HRTEM studies showed high density of dislocations within the grains; the dislocations comprised (100) and (110) edge dislocations with Burger vector of $d_{(100)}$ and $d_{(110)}$ respectively. Zr doping promoted atomic level homogenization and a uniform distribution of Nd and Sr in the lattice, inducing greatly enhanced carrier mobility. Transport property measurements showed a significant increase in power factor, mainly resulting from the enhanced electrical conductivity while the Seebeck coefficients were unchanged. In optimised samples a power factor of 2.0×10^{-3} W m^{-1} K^{-2} was obtained at 500 K. This is a ~ 30% improvement compared to the highest values reported for $SrTiO_3$–based ceramics. The highest ZT value for $Sr_{0.9}Nd_{0.1}TiO_3$ was 0.37 at 1015 K. This paper demonstrates the critical importance of controlling the structure at the atomic level and the effectiveness of minor dopants in enhancing the thermoelectric response.

Introduction

Oxide materials are promising for high temperature thermoelectric applications due to thermal and chemical stability at high temperatures in both oxidising and inert atmospheres. Candidate materials are frequently screened by evaluating the dimensionless thermoelectric figure of merit, $ZT = \frac{\sigma S^2}{\kappa} T$; where σ is electrical conductivity, S is Seebeck coefficient and κ thermal conductivity. To maximise ZT requires a simultaneous increase in electrical conductivity and decrease in thermal conductivity, although the two parameters are intimately linked. Following early work on layered cobaltites a wide variety of different oxides have been investigated with n-type thermoelectrics including $SrTiO_3$,[1] $CaMnO_3$,[2] $Zn_{0.96}Al_{0.02}Ga_{0.02}O$,[3] Magnelí phase oxides (TiO_{2-x},[4] $WO_{2.9}$[5] and $Nb_{12}O_{29}$[6]), tungsten bronze structured oxides ($Ba_{5.19}Nd_{8.54}Ti_{18}O_{54}$[7]) and homologous series oxides ($In_2O_3(ZnO)_m$[8] and $Ga_2O_3(ZnO)_m$[9]). The most promising p-type thermoelectric oxides include $Na(Co_{0.95}Cu_{0.05})_2O_4$,[10] $Ca_3Co_4O_9$,[11] and $Bi_2Sr_2Co_2O_x$[12].

The n-type $SrTiO_3$ has attracted considerable interest because of its high Seebeck coefficient and the fact that the power factor of single crystal material is comparable to that of Bi_2Te_3[1] employed in commercial thermoelectric devices. However, the high lattice thermal conductivity of polycrystalline $SrTiO_3$ is still a drawback ($\kappa > 3$ W m^{-1} K^{-1} at 1000 K),[13] and the small mean-free-path of phonons (≈ 2 nm at 1000 K) limits use of nanostructuring as a route to reduce thermal conductivity.[6] In general, the highest ZT values for $SrTiO_3$ have been achieved by sintering at high temperatures for extended sintering periods under reducing atmospheres. The collected results of studies on the effects of different dopants and doping conditions (summarised in Figure S.1, supplementary information) showed that the optimum concentration for A-site doping was ~10 at.% and preferably with dopants from lanthanide series of elements.[13–22] In this regard, doping $SrTiO_3$ with lanthanides having greater ionic radii (La, Pr, etc.) tends to lead to an increased power factor as a result of reduced carrier localisation.[13–17,19,20,22] In contrast, doping with smaller ionic radii lanthanides (Gd, Dy, etc.) tends to result in lower thermal conductivity because of the increase in mass and strain contrast.[13,15,18,21] For example Liu et al.[14] showed that Nd doping at 10 at.% simultaneously improved the ZT value of $SrTiO_3$ by enhancement of power factor and reduction of thermal conductivity. Subsequently Kovalevsky et al.[13] and Liu et al.[14] further increased the power factor of $SrTiO_3$ by inclusion of 10 at.% Nd, and Kovalevsky et al.[13] showed that annealing in a strongly reducing atmosphere (10%H$_2$-90%N$_2$) would lead to a further improvement in power factor. The highest power factor among Nd-doped $SrTiO_3$ studies reported thus far is ~1.55×10^{-3} W m^{-1} K^{-2} at 673 K and the highest ZT value reported is 0.39 for $Sr_{0.9}Nd_{0.1}TiO_3$ at 1073 K.[13] For many applications increasing the power factor is more valuable than simply increasing ZT as the power output (P_{out}) is directly related to the power factor (Equation 1) whereas the relationship between the efficiency (η) and ZT is not as straightforward (Equation 2).[23,24] For instance, increasing the power factor by 25%

leads to 25% improvement in P_{out} while there is only 11.1% improvement in η when ZT is improved from 0.37 to 0.42.

$$P_{out} = \frac{\sigma S^2 (\Delta T)^2}{4} \tag{1}$$

$$\eta = \frac{T_H - T_C}{T_H} \left\{ \frac{\sqrt{1 + \overline{ZT}} - 1}{\sqrt{1 + \overline{ZT}} + {T_C}/{T_H}} \right\} \tag{2}$$

where; $\Delta T = T_H - T_C$, T_H is the hot side temperature, T_C is the cold side temperature and $\overline{ZT}$ is the average ZT of the module.

The objective of the present study was therefore to improve the thermoelectric properties, or more specifically the power factor, of 10 at.% Nd-doped $SrTiO_3$ by using minor additives to control the microstructure and transport properties. We selected B_2O_3 to promote liquid phase sintering, thereby improving sinterability at lower temperatures. The amount of B_2O_3 was determined from earlier studies[25] which suggested that 0.5 wt.% addition was sufficient for the preparation of dense ceramics. ZrO_2 was used to modify the electronic properties of Nd-doped $SrTiO_3$ while maintaining acceptable thermal conductivity. It was also anticipated that ZrO_2 additions could improve carrier mobility.[26,27] One of the few studies on the effect of ZrO_2 additions[27] suggested that zirconia increased carrier mobility, but reduced sinterability when the amount of ZrO_2 addition was greater than 1 wt.%. By adding small amounts of both B_2O_3 and ZrO_2 we sought to improve both microstructure development and transport properties. By the addition of 0.5 wt.% B_2O_3 and 0.3 wt.% ZrO_2, the thermoelectric power factor was increased by nearly 30% and ZT was at least comparable to the previously reported work on $Sr_{0.9}Nd_{0.1}TiO_3$. The significant improvements were a consequence of the modification and control of microstructure and chemical homogeneity of the material.

Experimental

Synthesis and Processing of $Sr_{0.9}Nd_{0.1}TiO_3$

Samples of $Sr_{0.9}Nd_{0.1}TiO_3$ were synthesised by conventional mixed oxide techniques using $SrCO_3$ (Sigma Aldrich, >99.9%), TiO_2 (Sigma Aldrich, ≥99.9%) and Nd_2O_3 (Π-KEM, >99.9%) powders. Nd_2O_3 powders were dried in air at 1173 K for 6 hours prior to weighing. The starting powders were wet-milled for 24 hours using zirconia media and propan-2-ol then dried at 363 K for 24 hours. The mixed powders were calcined in air at 1473 K for 8 hours using an alumina crucible. Dopants (0.5 wt% B_2O_3 and x wt% ZrO_2; x=0, 0.2, 0.3, 0.4 and 0.8) were added and the same milling and drying procedures were then used to homogeneously mix the additives with calcined powders. The resulting powders were uniaxially pressed at ~50 MPa to form cylindrical pellets 20 mm in diameter and then sintered in 5%H_2-95%Ar atmosphere at 1673 K between 4 and 24 hours. Since all the formulations

contain 0.5 wt% of B_2O_3, hereafter the B_2O_3 content will not specified; only the ZrO_2 content will be mentioned. The sample codes are listed in Table 1.

Table 1 Sintering times, additive levels and samples codes

Composition	Additives	Sintering time	Sample Code
	0.5 w.% B_2O_3	12 hours	0Z-12h
	0.5 w.% B_2O_3 + 0.2 wt.% ZrO_2	12 hours	2Z-12h
	0.5 w.% B_2O_3 + 0.3 wt.% ZrO_2	12 hours	3Z-12h
$Sr_{0.9}Nd_{0.1}TiO_{3\pm\delta}$	0.5 w.% B_2O_3 + 0.4 wt.% ZrO_2	12 hours	4Z-12h
	0.5 w.% B_2O_3 + 0.8 wt.% ZrO_2	12 hours	8Z-12h
	0.5 w.% B_2O_3 + 0.3 wt.% ZrO_2	4 hours	3Z-4h
	0.5 w.% B_2O_3 + 0.3 wt.% ZrO_2	24 hours	3Z-24h

Characterisation

Phase analysis was undertaken with a Philips X'Pert diffractometer with a Cu-Kα source (λ=1.540598 Å); diffraction patterns were collected between 20° to 80° using a step size of 0.005 and a dwell time of 7 seconds/step. Diffraction patterns for selected samples were also obtained using Synchrotron X-ray powder diffraction (SXPD) on beam line I11 at the Diamond Light Source, UK.[28] High resolution SXPD patterns (0.001° data binned size) were recorded using multi-analyser crystal (MAC) detectors. Structural details were obtained from data refinements using TOPAS 5.0 Software.[29]

The microstructures of the polished sample surfaces were investigated using a Philips XL30 FEG-SEM equipped with an energy dispersive X-ray (EDX) detector. Bar shaped samples were cut from the sintered pellets and ground using SiC papers down to 4000-grade. The surface was further polished using 1 and ¼ μm diamond paste to achieve mirror-like finish; final polishing was carried out using a colloidal solution of silica suspension (OPS). The average grain size was determined using linear intercept method of Mendelson.[30]

Samples for TEM and STEM investigation were prepared by both standard crushing and ion beam thinning techniques. For the crushing method, the sintered disks were crushed to powder using an agate mortar and pestle. Grains of individual powders were dispersed in chloroform, dropped onto a copper grid covered with a holey carbon film, and then dried. For ion beam-thinning, specimens were first ground on 1200 grade SiC to reduce the thickness to ~300 μm. They were ultrasonically cut into 3 mm diameter disks (Model KT150; Kerry Ultrasonic Ltd.) then dimpled (Model D500; VCR Group, San Francisco, CA) to reduce the thickness of the centre of the disk to 30 μm. Finally, the disks were ion beam thinned (using a Gatan precision ion polishing system model 691; PIPS™) operating at 4–6 kV. Structures were initially investigated using selected area electron diffraction (SAED) and high-

resolution transmission electron microscopy (HRTEM) techniques using a FEI FEGTEM (Tecnai G2, Hillsboro, OR) operating at 300 kV. Subsequently, atomic level resolution level structural characterization was carried out using an aberration-corrected Nion microscope (UltraSTEM100; Nion Company, Kirkland, WA) located at the Daresbury SuperSTEM Laboratory in the United Kingdom.

X-ray photoelectron spectroscopy (XPS) patterns were obtained by a Kratos Axis Ultra spectrometer with monochromatic Al Kα radiation (E_{source}= 1486.69 eV). XPS binding energies were calibrated using C 1s peak (284.8 eV). Peak fitting was carried out using the CASA XPS program, which allowed the determination of FWHM, peak location, and optimal peak shape within the data constraints using a mix of Lorentzian and Gaussian characters.

The electrical conductivity and the Seebeck coefficients of the samples were determined simultaneously using bar shaped samples (2.5x2.5x15 mm^3) with an ULVAC ZEM-3 facility between 300 and 1050 K in a low pressure He atmosphere.

The thermal conductivity ($\kappa=\alpha\rho C_p$) of the samples was determined from thermal diffusivity (α), density (ρ) and the specific heat capacity (C_p) data. The thermal diffusivity was determined using laser flash method in Ar atmosphere with a NETZCH LFA-427, while the specific heat capacity was obtained by differential scanning calorimetry (DSC) with a Netzsch STA 449C in Ar atmosphere. These measurements were undertaken between 300 and 1050 K. The densities of the samples were deduced from mass and dimension measurements.

Results and Discussion

Bulk Properties

All the ceramic samples were high density (> 95% theoretical), crack-free and dark grey in colour. The incorporation of 0.5 wt% B_2O_3 in the starting materials enabled effective synthesis by a liquid phase sintering mechanism, and reduction in the processing temperature by 50 to 150 K compared to many earlier studies.[13−15,31] Boron oxide is well established as a processing aid for electroceramics,[25] but when it was used as a dopant in single crystal SrTiO$_3$, it was shown to improve the electrical conductivity,[32] hence an additional reason for its use here.

Phase Analysis

From initial structural characterisation, using laboratory X-Ray Diffraction, all the Sr$_{0.9}$Nd$_{0.1}$TiO$_3$ ceramics (0Z to 8Z) were single phase (Figure S.2, supplementary information). The effect of ZrO$_2$ additions on the structure of the samples was examined by synchrotron X-ray powder diffraction (SXPD). The ceramics sintered for 12 hours had tetragonal structure ($a_t \approx \sqrt{2}a_p$ and $c_t \approx 2a_p$ with space group I4/mcm) irrespective of ZrO$_2$ content. This was apparent from the splitting of (200)$_p$ peak and the

5

appearance of a weak reflection corresponding to anti-phase tilting of TiO_6 octahedra as shown in Figure 1a. The changes in lattice parameters obtained by Rietveld refinement of the SXPD pattern are presented in Figure 1b and Table S.1 (supplementary information). With increasing ZrO_2 additions, the peak positions were displaced to lower angles reflecting the net increase in unit cell volume. This could be linked to the reduction of titanium from $Ti^{4+} \rightarrow Ti^{3+}$ (ionic radii: $R_{Ti^{4+}}=0.605$ Å and $R_{Ti^{3+}}=0.67$ Å), and the formation of oxygen vacancies under reducing conditions.[33,34] It could also result from the substitution of Zr into the host matrix as observed in earlier studies;[35] however, it is hard to estimate the degree of substitution of Zr into the perovskite lattice. As expected the unit cell volumes for $Sr_{0.9}Nd_{0.1}TiO_3$ samples were smaller than for the $SrTiO_3$ ($a_P=3.905$ Å) base material, confirming the successful substitution of the smaller Nd for Sr on the perovskite A-site ($R_{Sr^{2+}}=1.31$ Å and $R_{Nd^{3+}}=1.16$ Å[36]). The lattice parameters for $Sr_{0.9}Nd_{0.1}TiO_3$ (Figure 1b) are comparable to those reported previously.[13,14]

Our initial study showed the addition of 0.3 wt.% ZrO_2 to be optimum for improving the thermoelectric properties. Thus, the effect of sintering time (4, 12 and 24 hours) on this formulation was investigated. Figures S.3 and S.4 (see supplementary information) show the Cu-radiation XRD patterns and Rietveld refinements for the samples; the variation in lattice parameter with sintering time is presented in Figure 1c. The 3Z samples sintered for less than 12 hours exhibited a mixture of cubic ($Pm\overline{3}m$) and tetragonal (I4/mcm) structures while the samples sintered for 12 and longer were single phase with tetragonal structure (I4/mcm). The cubic structure for $Sr_{0.9}Nd_{0.1}TiO_3$ had previously been reported[14] while the most recent studies suggested a tetragonal structure.[13] Our data clarifies the apparent discrepancy between the earlier studies since a shorter sintering time leads to a cubic structure, but then changes to tetragonal with prolonged heat treatment. This change in the crystal symmetry with sintering time can be linked to the increase in oxygen deficiency content with sintering time. Gong et al.[37] showed that with increasing oxygen deficiency, $SrTiO_{3-\delta}$ crystals developed a tetragonal crystal structure.
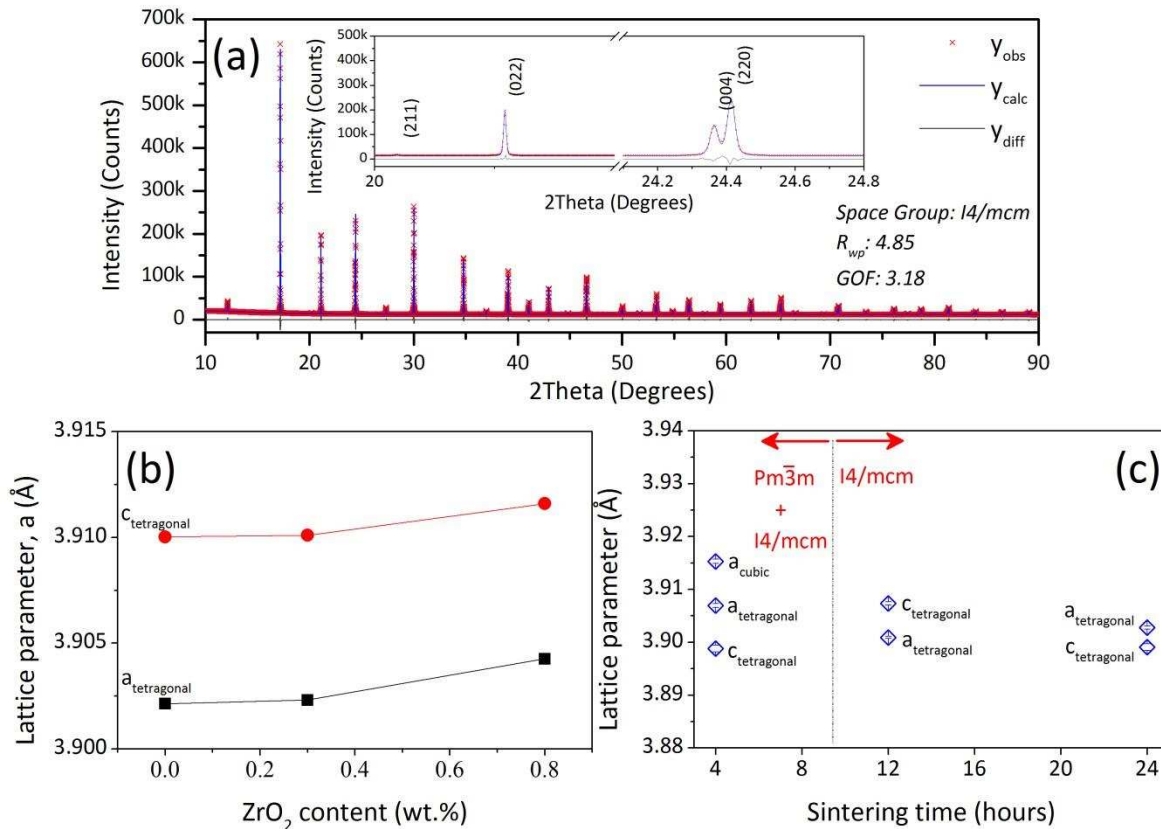
Figure 1 (a) Full profile Rietveld refinement of SXPD *(λ=0.825939(10) Å)* data for $Sr_{0.9}Nd_{0.1}TiO_3$ prepared with 0.3 wt.% ZrO_2 (i.e. 3Z); **(b)** lattice parameters as a function of ZrO_2 content; **(c)** lattice parameters as a function of sintering time for samples 3Z. Uncertainty bars are included but are smaller than the symbol size.

Microstructure and Nanostructure

SEM back scattered electron (BSE) micrographs $Sr_{0.9}Nd_{0.1}TiO_3$ samples prepared with different amounts of ZrO_2 (sintered for 12 hours) are shown in Figure 2. For the 0Z-12h sample, grain inhomogeneity was observed with localised fine grain clusters (highlighted by red arrows in Figure 2a). However, increasing ZrO_2 content to 0.3 wt% led to a relatively homogeneous microstructure with narrow grain size distribution and average grain size (~52 μm) as seen in Figure 2b. Further increase in ZrO_2 level to 0.8 wt% inhibited the grain growth, which resulted in a much smaller grain size (~7.0 μm) but with significant variation, as highlighted by blue arrows in Figure 2c. The effect of sintering time on the microstructure was limited, with the average grain size varying between 46 and 59 μm for the samples sintered for up to 24 hours (see Figures S.5 and S.6 in supplementary information for micrographs and grain size distributions). There was no evidence of secondary phases, confirming the single phase nature of the samples. Finally, domain-like features, due to the phase transformation from high symmetry structures formed at high temperature to lower symmetry structure at room temperature,[38] are shown in Figure 2d. The width of these features typically are >1μm for all the samples

irrespective of ZrO_2 content, which is larger than phonon mean free path for $SrTiO_3$ (typically <10 nm).[39] In order to act as phonon scattering centres and reduce thermal conductivity, it is generally suggested that maximum domain size should be ~20 nm.[40] Therefore, these domain features are not expected to have a significant effect on the thermal transport properties.
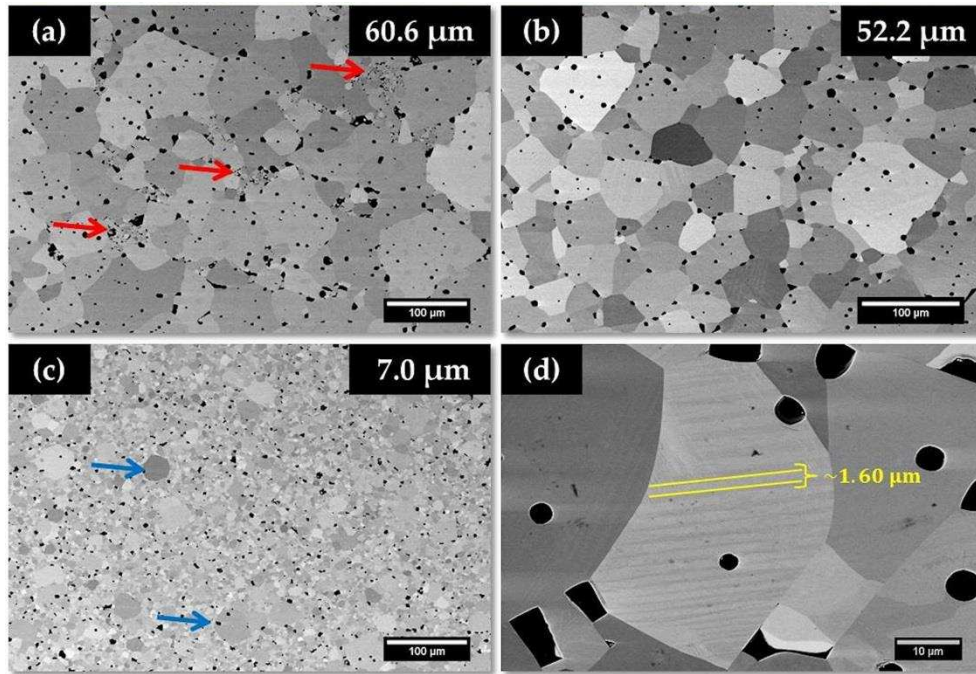

Figure 2 SEM-BSE micrographs showing the effect of ZrO_2 content on the microstructure of (a) 0Z-12h, (b) 3Z-12h, (c) 8Z-12h samples. (d) Higher magnification micrograph showing the domain-like features observed in 3Z-12h sample

SAED patterns for the samples prepared with different ZrO_2 content were collected along $[001]_p$, $[110]_p$ and $[111]_p$ zone axes to confirm the crystal structure of the samples (Figure 3 for 3Z samples and Figure S.7 for 0Z, 3Z and 8Z samples). Only reflections corresponding to aristotype structure were present in the patterns along $[001]_p$ and $[111]_p$ zone axes. However, $\frac{1}{2}\{ooo\}$ type reflections (labelled as "t" on the patterns) were present in $[110]_p$ zone axis. This type of reflections is due to antiphase tilting of the TiO_6 octahedra and indicates that the tilt system for the samples to be $a^0a^0c^-$, according to Glazer's notation.[41] Thus the crystal structure for the samples heat treated for 12 hours was confirmed to be tetragonal with I4/mcm space group,[42] consistent with XRD data (Figure 1c and Figure S.3 in supplementary information).
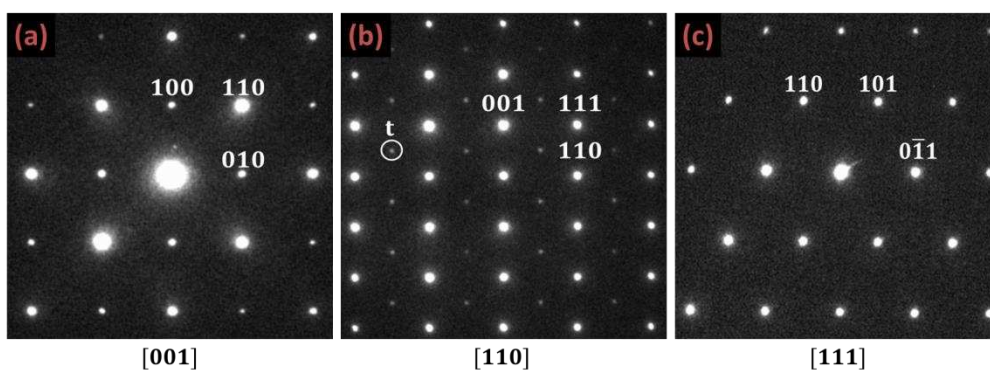
Figure 3 SAED patterns along major zone axes for 3Z-12h sample

HRTEM imaging was employed to analyse the sub-grain features with respect to ZrO_2 content. A high density of dislocations was present in the samples irrespective of ZrO_2 content (Figure S.8 in supplementary information).The nature of the dislocations was analysed using HAADF (averaged by non-rigid registration[43]) techniques and by applying Inverse Fourier Transformation (IFFT) to the dislocation core (as presented in Figure 4a-c). The application of IFFT revealed lattice fringes along (100) and (011) planes (Figure 4a-b), confirming the presence of a complex dislocation core. These edge dislocations had Burgers' vectors (BV) of $\frac{1}{2}d_{(110)cubic}$ and $\frac{1}{2}d_{(100)cubic}$, respectively (Figure 4c). This is the first observation of complex dislocation cores in an oxygen deficient polycrystalline $SrTiO_3$ based ceramic and is consistent with reports on the dislocation core structures for $SrTiO_3$.[44-48] This work has shown that in the core region there will be localised variation in site occupancies, rearrangements of Ti-O octahedra and the appearance of Ti on Sr sites due to a different configuration of edge sharing octahedra. The presence of such configurations is highlighted by the arrows in Figure 4c. This chemically composite nature of the dislocations and its possible effect on both electrical and thermal conductivity will be discussed later.
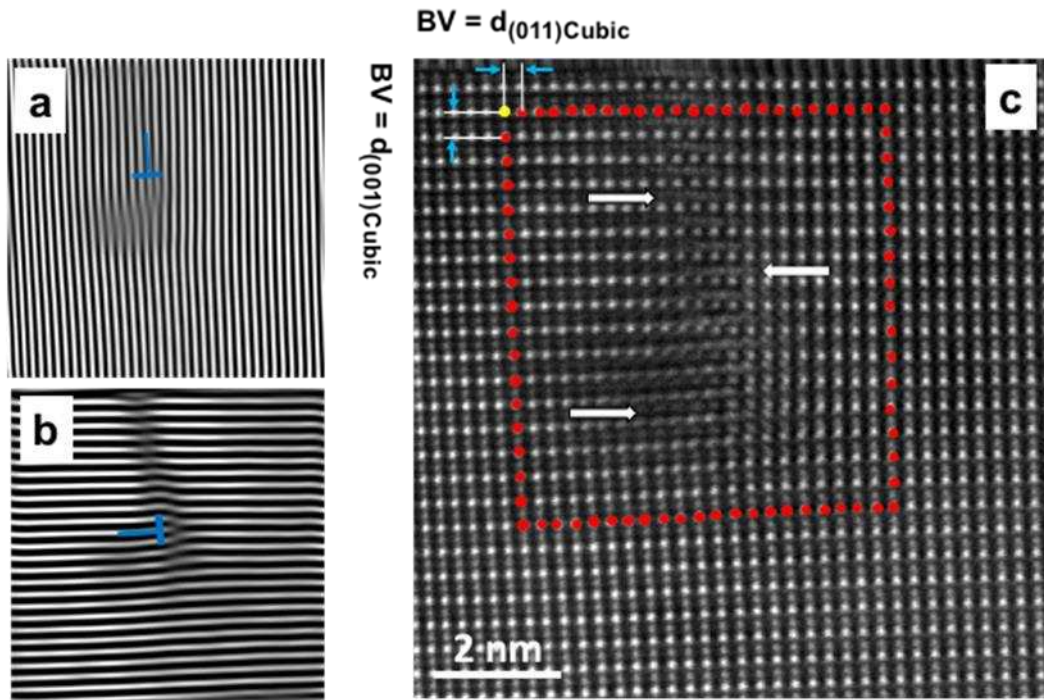
Figure 4 IFFT from **(a)** (100) and **(b)** (011) reflections of the dislocation core shown in (c) HAADF image along [110] zone axis of 0Z-12h sample

Another important observation from HRTEM was the presence of nano-inclusions, typically 5nm in size, in the 0Z-12h samples. Examples of the nano-inclusions are presented in the low magnification TEM image of $[001]_p$ zone axis (Figure 5a). Figure 5b-e presents $[110]_p$ zone axis HRTEM image, SAED pattern and Fourier Transformation (FFT) from the matrix and inclusion. Both the matrix and inclusions exhibit the same main reflections indicating both have a similar crystal structure. However, extra reflections around $\frac{1}{2}(1\bar{1}1)$ reflections of $[110]_p$ exist in the FFT of the inclusion, arrowed in Figure 5d and in the SADP arrowed in Figure 5e. The presence of extra reflections indicated the existence of a superlattice structure in the inclusion. In contrast to the observation of nano-inclusions in the 0Z-12h samples, the HRTEM study of 3Z-12h samples showed them to be single phase with no inclusions. As highlighted above, the presence of a high density of dislocations was a significant feature of the microstructure. The dislocations could have arisen as a consequence of liquid phase formation (generated by the additives[25,49]) enabling grain boundary migration[50,51] and resulting growth accidents.[52] Therefore, 0Z-12h and 3Z-12h samples were investigated using aberration corrected STEM (SuperSTEM[2], Daresbury facility).
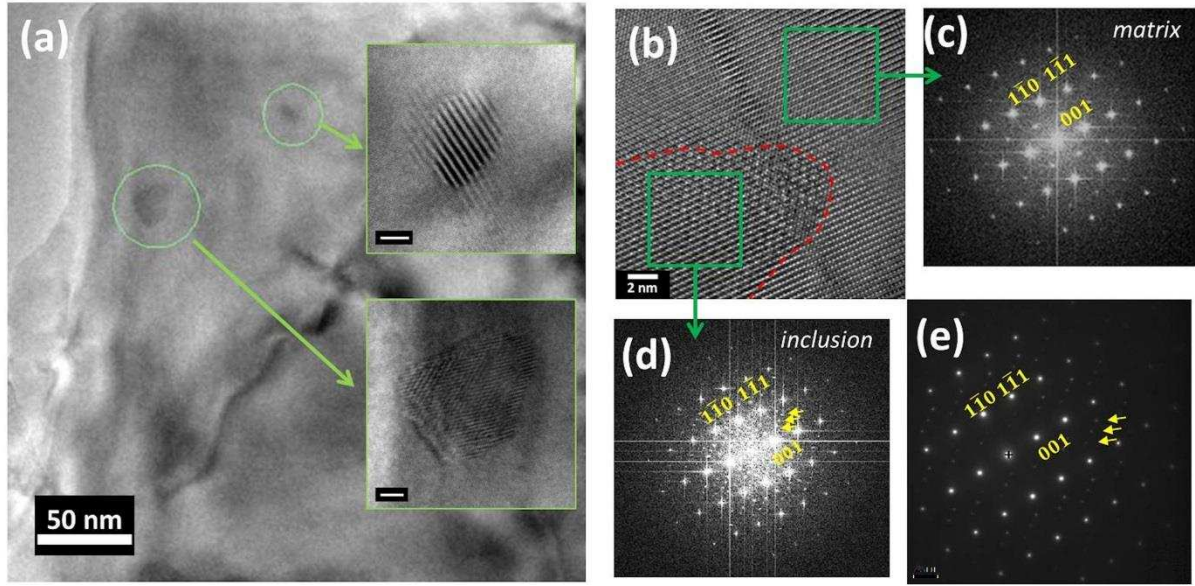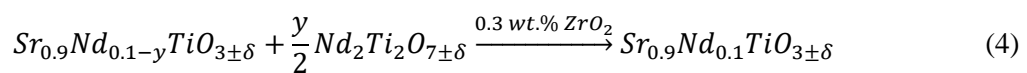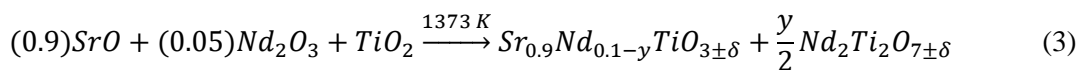
Figure 5 **(a)** HRTEM image showing the presence of precipitates in the sample for 0Z-12h sample; **(b)** HRTEM image and **(e)** [110]$_p$ zone axis SAED showing the extra reflections ; **(c)** and **(d)** the FFT from matrix and inclusion sections in the samples. Additional reflections from the inclusion are highlighted by arrows in both SAED and FFT.

HAADF images were collected along [001]$_p$ and [110]$_p$ zone axis and EELS maps were obtained for both 0Z-12h and 3Z-12h samples. The [001]$_p$ data are presented in Figure 6a-j. Ti L$_{2,3}$ edge map for the sample without ZrO$_2$ addition (Figure 6c) showed that the B-site is only occupied by Ti and its distribution is homogenous. The Nd M$_{4,5}$ EELS map, shown in Figure 6d, suggests that only Nd is distributed in the A-site. However, the distribution is non-uniform. This observation was the case for different areas from which data were collected. On the other hand, when 0.3 wt% ZrO$_2$ is added, both Nd and Ti are uniformly distributed in A- and B-sites, as shown in Figure 6h-i; in total contrast to the samples without addition of ZrO$_2$. Furthermore, the substitution of Nd into only A-sites was also confirmed since no Nd signal was detected from Ti columns. Therefore, it can be concluded that the presence of ZrO$_2$ in the starting formulation promotes atomic level chemical homogeneity in Nd-doped SrTiO$_3$ ceramics. The increased solubility of the Nd-rich phase in the SrTiO$_3$ matrix is encouraged by the formation of a liquid phase[26,27] upon ZrO$_2$ addition (Equations 3 and 4), which leads to the homogeneous distribution of Nd in the lattice.

$$(0.9)SrO + (0.05)Nd_2O_3 + TiO_2 \xrightarrow{1373\,K} Sr_{0.9}Nd_{0.1-y}TiO_{3\pm\delta} + \frac{y}{2}Nd_2Ti_2O_{7\pm\delta} \qquad (3)$$

$$Sr_{0.9}Nd_{0.1-y}TiO_{3\pm\delta} + \frac{y}{2}Nd_2Ti_2O_{7\pm\delta} \xrightarrow{0.3\,wt.\%\,ZrO_2} Sr_{0.9}Nd_{0.1}TiO_{3\pm\delta} \qquad (4)$$
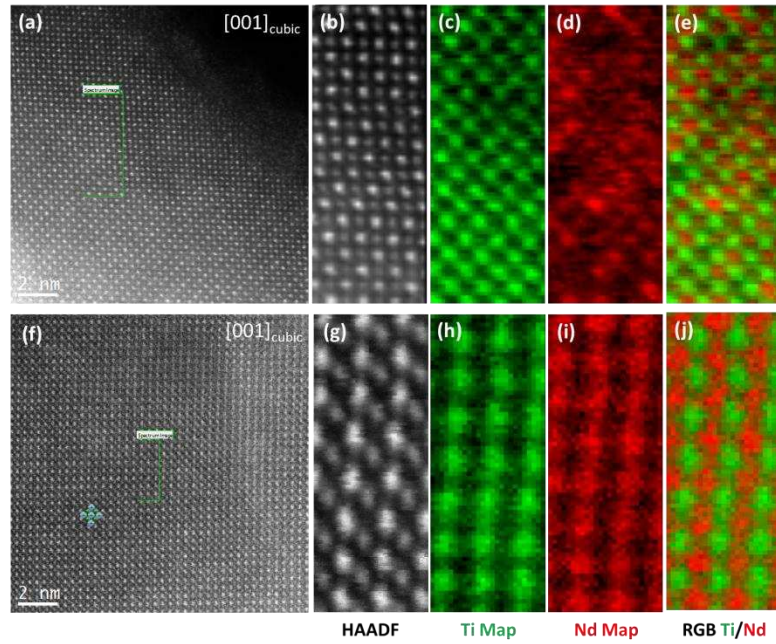
Figure 6 HAADF image along $[001]_p$ zone axis and corresponding HAADF image during data accusation and EELS maps from area of interest (green rectangle in the HAADF images) for the matrix phase of **(a-e)** 0Z-12h and **(f-j)** 3Z-12h samples

To reinforce the differences between samples prepared with and without zirconia, $[110]_p$ HAADF-EELS data for 0Z-12h samples are presented in Figure 7a-f. The area for data collection contains both the matrix phase and the inclusion (green rectangle in the HAADF image). It can be seen from the HAADF image in Figure 7b that there is no change in the ordering of atomic columns between the matrix and the inclusion. This was the case for the HAADF images collected along $[001]_p$ zone axis suggesting that the inclusion may have a perovskite type crystal structure. Alternatively, EELS maps revealed that there is difference in Ti, O and Nd signal from the matrix and inclusion, which is richer in content of these elements in the inclusion. Based on these observations the secondary phase precipitates is inferred to be a neodymium titanate based compound and probably $Nd_2Ti_2O_7$ which was detected in the XRD pattern of calcined powders before the final sintering.
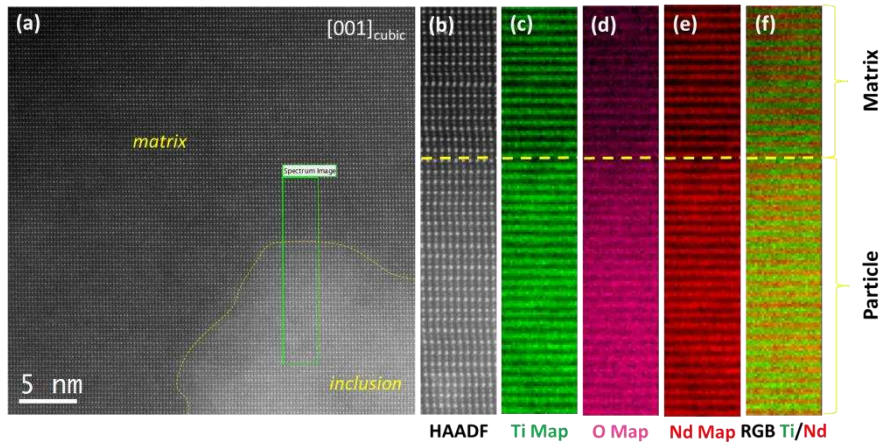
Figure 7 $[001]_p$ HAADF-EELS data for 0Z-12h sample; **(a)** HAADF image from the matrix and the inclusion, (b) HAADF image during accusation of EELS **(c)-(f)** EELS maps from area of interest using Ti $L_{2,3}$, O K and Nd $M_{4,5}$ edges.

X-ray Photoelectron Spectroscopy

High resolution XPS were collected to determine the concentration of Ti^{3+} in the samples. The Ti 2p spectra for the 3Z-12h sample, which is typical for all the samples, is presented in Figure 8. The Ti $2p_{3/2}$ and $2p_{1/2}$ core levels are due to 4+ and 3+ oxidation states in the samples. As expected, spin orbital splitting ($\Delta_{s.o.}$) of $2p_{3/2}$ and $2p_{1/2}$ core levels are ~5.7 eV for all the samples;[53–55] Ti 2p doublet peaks for Ti^{4+} are located at approximately 458.4 (Ti^{4+} $2p_{3/2}$) and 464.1 (Ti^{4+} $2p_{1/2}$) eV, which is similar to previous data for $SrTiO_3$.[53,56,57] The XPS results showed that the $[Ti^{3+}]$ content in samples prepared with with ZrO_2 additions up to 0.8 wt% was 5.9±0.4 %. Analysis of the samples for the optimised composition (0.3 wt% ZrO_2 addition) as a function of sintering time yielded a marginally lower, but not significantly different $[Ti^{3+}]$ content of 5.6±0.2 %. The variation in Ti^{3+} concentration is expected to have a limited effect on carrier concentrations.
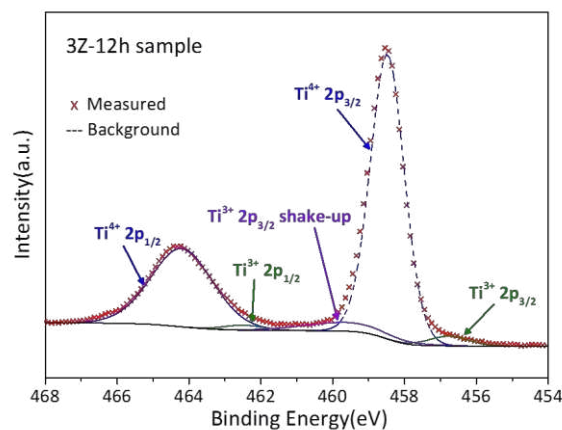

Figure 8 Ti 2p high-resolution XPS spectra of the sample with 0.3 wt% ZrO_2 addition

13

Thermoelectric Properties

Electronic transport properties are presented in Figure 9. It is clear that electrical conductivity (Figure 9a) and power factor (Figure 9c) are sensitive to ZrO_2 content, achieving maximum values for the samples prepared with 0.3 wt% ZrO_2. In contrast, the Seebeck coefficients (Figure 9b) are insensitive to zirconia content. The samples, except for 0Z-12h, exhibited metallic type conduction behaviour above room temperature while semiconductor-like behaviour was observed for the 0Z-12h sample and the rest of the samples near room temperature. This type of temperature dependency is typical for $Sr_{0.9}Nd_{0.1}TiO_3$ ceramics and linked to the distortion of the lattice[14] and also the formation of high-ohmic depletion layers.[13] At 313 K the electrical conductivity increased from 40 S cm^{-1} (0Z-12h) to 1420 S cm^{-1} with only 0.3 wt% ZrO_2 addition, while it had a less pronounced effect at high temperatures (Figure S.9a in supplementary information). This suggests that grain boundary scattering is dominant at low temperatures, since the variation of electrical conductivity with microstructure (due to changes in ZrO_2) content was limited to these temperatures.[58] These trends are consistent with the earlier investigations of the effect of yttria stabilised zirconia (YSZ) addition on thermoelectric properties of $SrNb_{0.15}Ti_{0.85}O_3$ ceramics.[27,59] However, the use of much higher additions of YSZ (up to 5 mole%) led to samples of much lower density. Thus, co-doping zirconia with B_2O_3, which is a proven beneficial sintering aid, eliminates the densification problems and has proven very effective since low level additions of ZrO_2 have enabled improvement of thermoelectric properties. Moreover, it was previously shown that the presence of dislocations can promote oxygen vacancy formation due to strain fields,[48] and thereby enhance electrical conductivity through increasing the carrier concentration. As a result there was a substantial improvement in the power factor (Figure 9c). The maximum power factor increased nearly 10 fold from 0.2×10^{-3} to 2.0×10^{-3} W m^{-1} K^{-2} with only 0.3 wt% ZrO_2 addition (Figure S.9b in supplementary information). However, increasing ZrO_2 level to 0.8 wt% reduced the power factor to $\sim1.17\times10^{-3}$ W m^{-1} K^{-2}. The maximum power factor achieved in this study is the highest, by approximately 30% for polycrystalline $SrTiO_3$ based ceramics prepared with conventional methods (see Table S.2 in supplementary information for more detail); previously the highest value reported was $\sim1.55\times10^{-3}$ W m^{-1} K^{-2} for Nd-doped $SrTiO_3$.[13] Having noted the importance of power factor for selecting materials for practical applications, this is a particularly significant result.
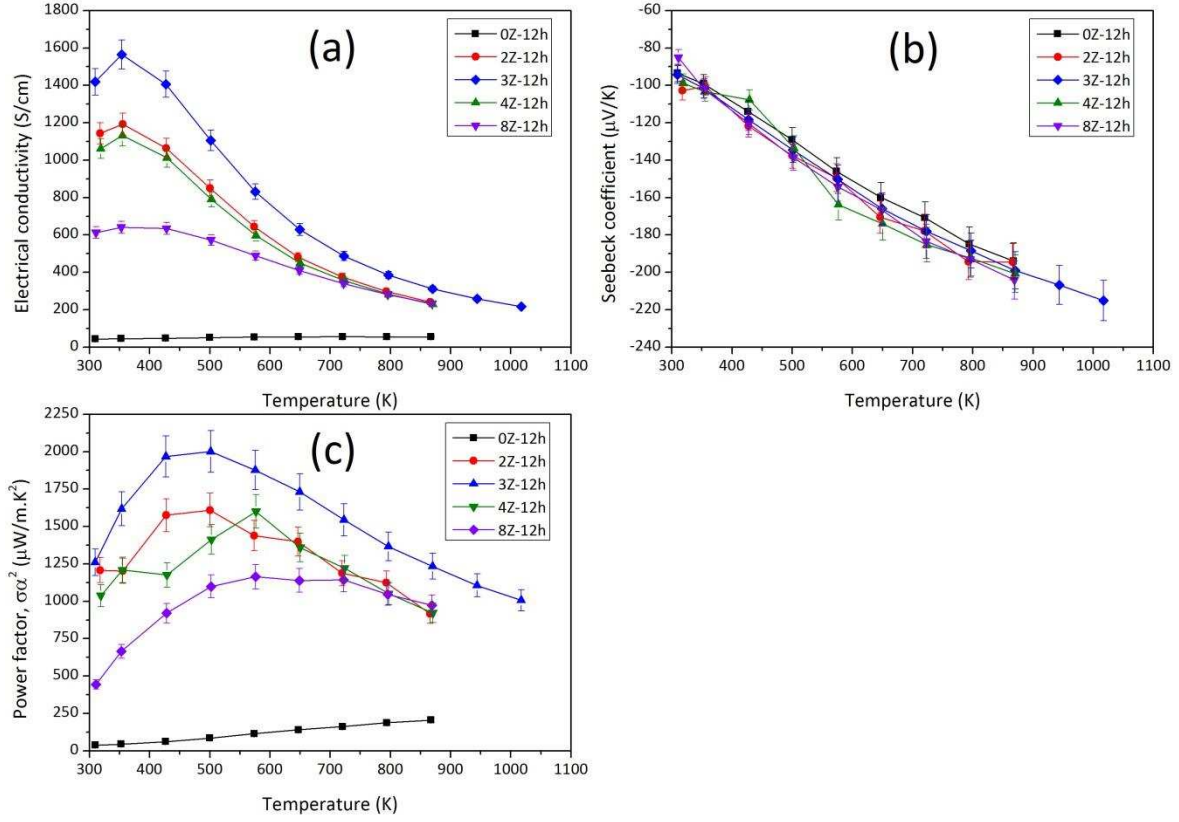
Figure 9 Electronic transport properties for $Sr_{0.9}Nd_{0.1}TiO_3$ samples prepared with different amounts of ZrO_2; **(a)** electrical conductivity, **(b)** Seebeck coefficient and **(c)** power factor.

The modified Heikes formula[60] for a tetragonal crystal structure (Equation 5) was used to calculate carrier concentration as a function of ZrO_2 content. With this data the usual conduction relationship (Equation 6) was utilised to calculate carrier mobility.

$$n = \frac{4}{V}\left\{\frac{1}{exp(\pm Se/k) + 1}\right\} \tag{5}$$

$$\sigma = ne\mu \tag{6}$$

where, n is carrier concentration; V is the unit cell volume; S is the Seebeck coefficient; e is elemental charge; k is the Boltzmann constant; σ is electrical conductivity and μ is carrier mobility. It was found (Table 2) that carrier concentration was independent of zirconia content, being approximately 4.2×10^{21} cm^{-3} for all the samples; this is consistent with the XPS data. However, μ changed dramatically with increasing ZrO_2 content, going from 0.065 (for 0Z-12h sample) to 2.11 cm^2 V^{-1} s^{-1} with only 0.3 wt% ZrO_2, and then reducing to 0.91 cm^2 V^{-1} s^{-1} at 0.8 wt% ZrO_2. This non-linear behaviour could be linked to changes in the microstructure with ZrO_2 content at both atomic and micro scale. The homogeneous distribution of Nd in the lattice means less variation in the periodic potential within the lattice, leading to reduced electron scattering and hence improved carrier mobility upon ZrO_2 addition. Additionally,

15

the increase in average grain size leads to a reduction in the concentration of grain boundaries and a net improvement in carrier mobility since grain boundaries act as scattering centres for charge carriers.[61]

Table 2 Carrier concentration and carrier mobility values for the samples obtained by modified Heikes formula

Sample	0Z-12h	3Z-12h	8Z-12h	3Z-4h	3Z-24h
Carrier concentration (10^{21} cm^{-3})	4.202	4.205	4.205	4.201	4.210
Carrier mobility (cm^2 V^{-1} s^{-1})	0.065	2.106	0.913	1.402	2.109

In view of the structural changes that occur as a function of sample processing time, the effect of sintering time on thermoelectric properties were examined, and are presented in Figure 10. These samples also exhibited a metallic conduction behaviour above 400 K, agreeing with the previous work on donor doped $SrTiO_3$.[13,62] Furthermore, electrical conductivity increased with increasing sintering time. However, this improvement was mostly limited to low temperature region (Figure 10a). On the other hand, the Seebeck coefficients decreased linearly with temperature, varying between -80 and -220 μV K^{-1} (Figure 10b). The only difference was the deviation from linear decrease in S with temperature for the 3Z-4h sample, which could be linked to the presence of ionised impurities.[31] The calculated values for n ($\sim$4.21$\times10^{21}$ cm^{-3}) were independent of sintering time while μ increased from 1.40 to 2.11 cm^2 V^{-1} s^{-1} with increasing sintering time (Table 1). This also shows that variation in the electronic properties is due to changes in the microstructure. Finally, increasing sintering time led to an increase in power factor in parallel to an improvement in σ while S was maintained (Figure 10c). The highest power factor values were 1.7, 2.0 and 1.85 $\times10^{-3}$ W m^{-1} K^{-2} at $\sim$500 K for sintering times of 4, 12 and 24 hours, respectively (Figure S.10 in supplementary information). This is approximately 10-30% improvement using lower synthesis temperatures and shorter processing times in comparison to the highest power factor values for $Sr_{0.9}Nd_{0.1}TiO_3$ reported in the literature.[13] The data reported were reproducible between different samples and also between heating and cooling cycles; examples are presented in Figures S.11 and S.12 (supplementary information).
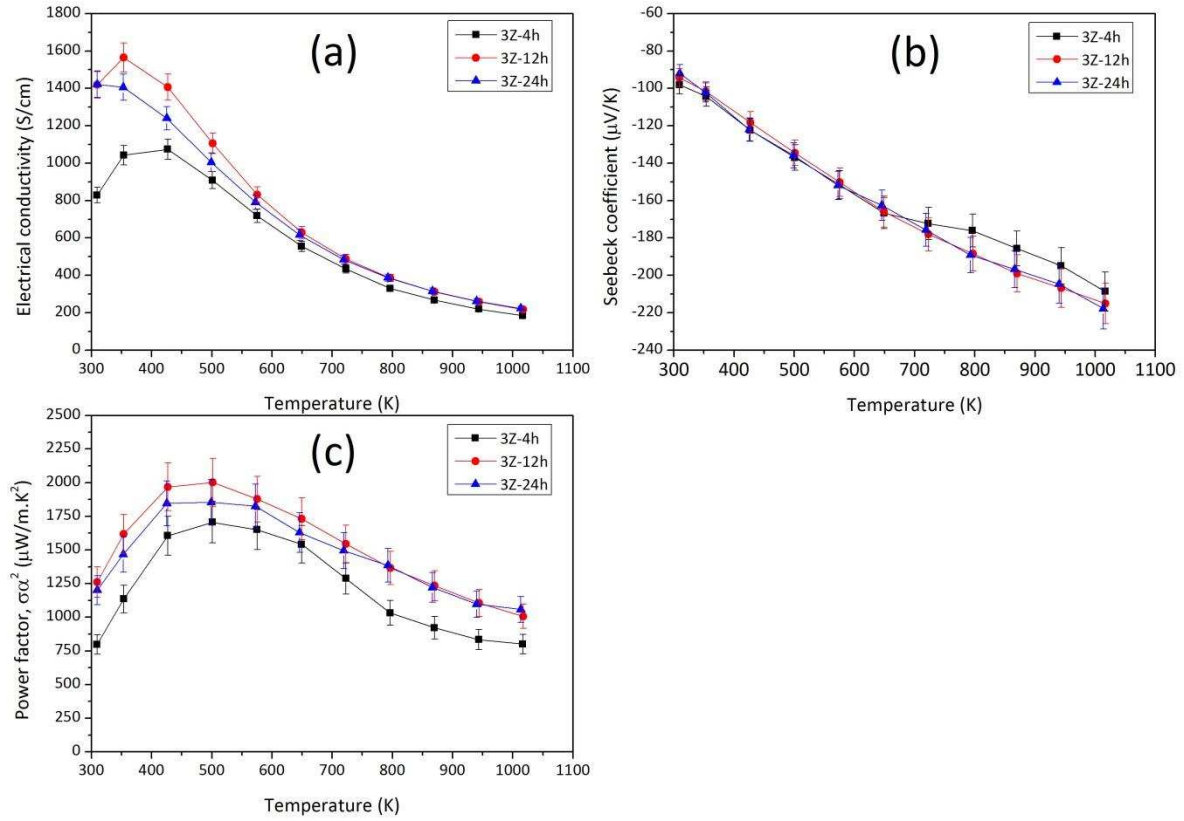
Figure 10 Electronic transport properties of 3Z samples prepared with different sintering times; **(a)** electrical conductivity, **(b)** Seebeck coefficient and **(c)** power factor.

The temperature dependence of total thermal conductivity (κ_{total}) of the optimised 3Z samples as a function of sintering time is shown in Figure 11a. At low temperatures there is a pronounced decrease in κ_{total} with temperature, which could be related to the boundary scattering of phonons, which tends to dominate at low temperatures.[63,64] Furthermore, the presence of dislocations (highlighted in the HRTEM images, Figure S.8 in supplementary information), could also help to reduce thermal conductivity by scattering phonons at low temperatures.[63–66] Overall, κ_{total} varies between 7.5 and 3.1 W m^{-1} K^{-1} for the samples and follows a T^{-1} dependency in the high temperature region due to Umklapp scattering.[67] The lattice and electronic components of thermal conductivity ($\kappa_{lattice}$ and $\kappa_{electron}$) were calculated using the Wiedemann–Franz law ($\kappa_{electron}= L\sigma T$; $L=2.44\times10^{-8}$ W Ω K^{-2}); results are presented in Figure 11b. The electronic contribution was at maximum 30% of the total and reduced to ~15% in the high temperature region. This low temperature contribution is significant in comparison to earlier work,[13] where the electronic component was less than 22% of the total. However, the presence of dislocations within grains could have helped to reduce $\kappa_{lattice}$.[68]
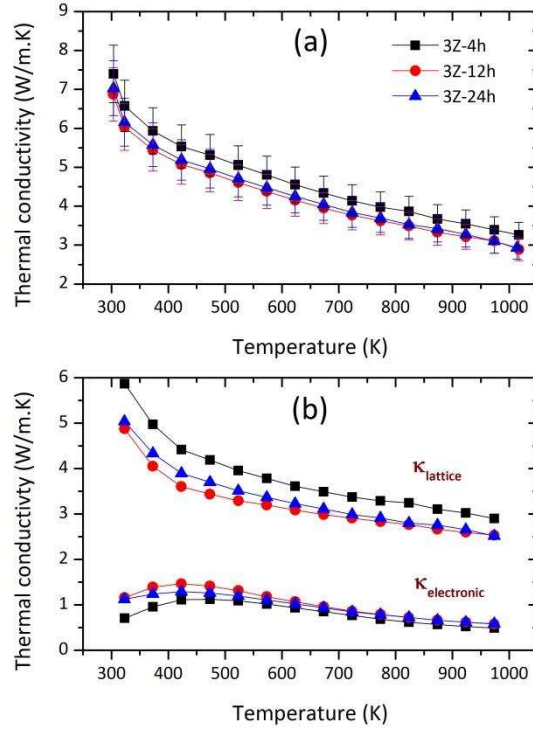
17

Figure 11 Temperature dependence of **(a)** κ_{total}, and **(b)** $\kappa_{lattice}$ *and* $\kappa_{electronic}$ of 3Z samples prepared with different sintering times from 4 to 24 hours

Based on the electronic and thermal transport properties, the thermoelectric figure of merit (ZT) values were calculated for the optimised 3Z samples (Figure 12). There was a significant increase in ZT as sintering time increased from 4 to 12 hours due to the noticeable decrease in |S|, but very little change for longer sintering times. The maximum ZT values achieved in this study for $Sr_{0.9}Nd_{0.1}TiO_{3\pm\delta}$-based ceramics (0.37 at 1015 K) are comparable with the data reported by Kovalevsky et al.[13] (0.39 at 1073 K). Although marginally higher ZT values (0.41 at 973 K) have been reported for $Sr_{0.775}La_{0.15}TiO_{3-\delta}$,[69] it is important to stress that the power factor increase for the present samples (30%) do represent a significant step forward. Indeed, from a practical stand point improvement in power factor by 30% is more beneficial than increasing the ZT value by 10%. While the output power of a module (P_{out}) is directly proportional to power factor the relationship between ZT and efficiency (η) is less direct.[24] For example, increasing in power factor by 30% will result in a 30% improvement in P_{out} whereas increasing ZT from 0.37 to 0.42 only leads to an 11% improvement in η.
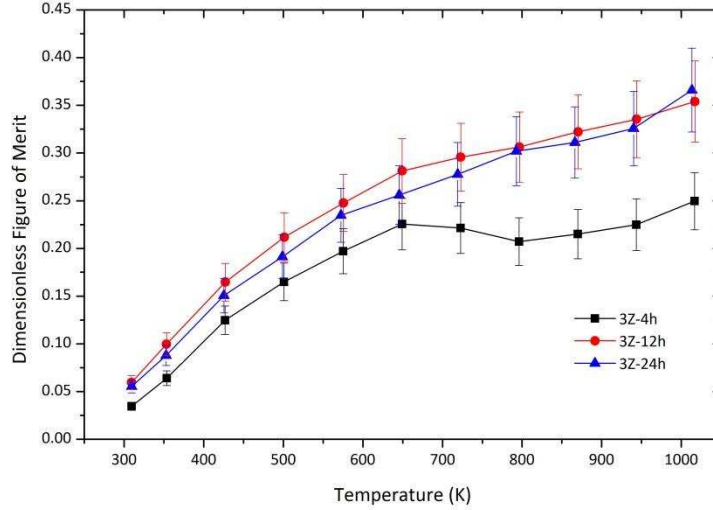
Figure 12 Temperature dependence of dimensionless figure of merit, ZT of 3Z samples prepared with different sintering times from 4 to 24 hours

Conclusions

This work presents important new information on the behaviour of a leading n-type thermoelectric oxide and a route to control structure and enhance transport properties. High density, high quality $Sr_{0.9}Nd_{0.1}TiO_{3\pm\delta}$ polycrystalline samples were synthesised by single step heat treatment in a reducing atmosphere with the aid of additives: B_2O_3 reduced the processing temperature through development of a liquid phase; ZrO_2 additions controlled the nanostructure, microstructure and thermoelectric properties. The average grain size decreased with increasing ZrO_2 addition; 0.3 wt% ZrO_2 provided most homogeneous grain size distribution.

HRTEM confirmed the I4/mcm tetragonal symmetry of the samples and the presence of a high density of dislocation irrespective of ZrO_2 content (0.0-0.8 wt%). In samples prepared without ZrO_2 additions, neodymium-rich precipitates (inferred to be $Nd_2Ti_2O_7$) were observed. However, ZrO_2 additions prevented the formation of such precipitates and also promoted atom level chemical homogeneity of Nd and Sr on the perovskite A sites. Additionally, complex dislocation cores in an oxygen-deficient, polycrystalline $SrTiO_3$ based ceramic were observed and analysed for the first time.

The incorporation of 0.3 wt% ZrO_2 dramatically improved the electrical conductivity of the samples without affecting the Seebeck coefficients. This resulted from the modification of microstructure at both grain and atomic scales by inhibiting the formation of nanoinclusions and also providing a homogeneous microstructure. As a consequence there was a significant increase in electrical conductivity; carrier mobility increased by a factor of 30 while there was a limited variation in carrier concentration. This led to a maximum power factor of 2.0×10^{-3} W m^{-1} K^{-2} at 500 K, which is nearly a

30% improvement over previous work on SrTiO$_3$-based ceramics. The maximum ZT was 0.37 at 1015 K. The significant (30%) enhancement of power factor achieved in the present study is more beneficial for practical applications than a modest increased in ZT value. The control of thermoelectric power factors through chemical homogeneity at the atomic level and microstructure scales could provide guidance in the routes to synthesise future target materials.

Conflicts of Interest

There are no conflicts to declare.

Acknowledgments

References

1   T. Okuda, K. Nakanishi, S. Miyasaka and Y. Tokura, Phys. Rev. B, 2001, **63**, 113104.

2   R. Funahashi, A. Kosuga, N. Miyasou, E. Takeuchi, S. Urata, K. Lee, H. Ohta and K. Koumoto, Int. Conf. Thermoelectr., 2007, 124–128.

3   M. Ohtaki, K. Araki and K. Yamamoto, J. Electron. Mater., 2009, **38**, 1234–1238.

4   S. Harada, K. Tanaka and H. Inui, J. Appl. Phys., 2010, **108**, 0–6.

5   G. Kieslich, C. S. Birkel, J. E. Douglas, M. Gaultois, I. Veremchuk, R. Seshadri, G. D. Stucky, Y. Grin and W. Tremel, J. Mater. Chem. A, 2013, **1**, 13050–13054.

6   M. Backhaus-Ricoult, J. Rustad, L. Moore, C. Smith and J. Brown, Appl. Phys. A Mater. Sci. Process., 2014, **116**, 433–470.

7   F. Azough, R. Freer, S. R. Yeandel, J. D. Baran, M. Molinari, S. C. Parker, E. Guilmeau, D. Kepaptsoglou, Q. Ramasse, A. Knox, D. Gregory, D. Paul, M. Paul, A. Montecucco, J. Siviter, P. Mullen, W. Li, G. Han, E. a. Man, H. Baig, T. Mallick, N. Sellami, G. Min and T. Sweet, J. Electron. Mater., 2016, **45**, 1894–1899.

8   H. Kaga, R. Asahi and T. Tani, Jpn. J. Appl. Phys., 2004, **43**, 3540–3543.

9   Y. Michiue, T. Mori, A. Prytuliak, Y. Matsushita, M. Tanaka and N. Kimizuka, RSC Adv., 2011, **1**, 1788.

10   H. Yakabe, K. Kikuchi, I. Terasaki, Y. Sasago and K. Uchinokura, *XVI ICT '97. Proc. ICT'97. 16th Int. Conf. Thermoelectr. (Cat. No.97TH8291)*, 1997, 523–527.

11   Q. M. Lu, J. X. Zhang, Q. Y. Zhang, Y. Q. Liu and D. M. Liu, Proceedengs Int. Conf. Thermoelectr. IEEE, 2006, 66–9.

12   E. Combe, R. Funahashi, F. Azough and R. Freer, J. Mater. Res., 2014, **29**, 1376–1382.

13   A. V Kovalevsky, A. A. Yaremchenko, S. Populoh, P. Thiel, D. P. Fagg, A. Weidenkaff and J. R. Frade, Phys. Chem. Chem. Phys., 2014, **16**, 26946–54.

14   J. Liu, C. L. Wang, W. B. Su, H. C. Wang, J. C. Li, J. L. Zhang and L. M. Mei, J. Alloys Compd., 2010, **492**, 54–56.

15   J. Liu, C. L. Wang, Y. Li, W. B. Su, Y. H. Zhu, J. C. Li and L. M. Mei, J. Appl. Phys., 2013, **114**, 223714.

16   A. V. Kovalevsky, A. A. Yaremchenko, S. Populoh, A. Weidenkaff and J. R. Frade, J. Appl. Phys., 2013, **113**, 053704.

17   A. M. Dehkordi, S. Bhattacharya, J. He, H. N. Alshareef and T. M. Tritt, Appl. Phys. Lett., 2014, **104**, 193902.

18   S. Bhattacharya, A. Mehdizadeh Dehkordi, S. Tennakoon, R. Adebisi, J. R. Gladden, T. Darroudi, H. N. Alshareef and T. M. Tritt, J. Appl. Phys., 2014, **115**, 223712.

19   Y. Kinemuchi, K. I. Mimura, A. Towata and K. Kato, J. Electron. Mater., 2014, **43**, 2011–2016.

20   A. M. Dehkordi, S. Bhattacharya, T. Darroudi, G. Jennifer W, U. Schwingenschlogl, H. N. Alshareef and T. M. Tritt, Chem. Mater., 2014, **26**, 2478–2485.

21   C. Chen, T. Zhang, R. Donelson, T. T. Tan and S. Li, J. Alloys Compd., 2015, **629**, 49–54.

22   A. M. Dehkordi, S. Bhattacharya, T. Darroudi, H. N. Alshareef and T. M. Tritt, J. Appl. Phys., 2015, **117**, 055102.

23   H. S. Kim, W. Liu and Z. Ren, J. Appl. Phys., 2015, **118**, 115103-1–9.

24   W. Liu, H. S. Kim, Q. Jie and Z. Ren, Scr. Mater., 2016, **111**, 3–9.

25   S. M. Rhim, S. Hong, H. Bak and O. K. Kim, J. Am. Ceram. Soc., 2000, **83**, 1145–1148.

26   N. Wang, H. Li, Y. Ba, Y. Wang, C. Wan, K. Fujinami and K. Koumoto, J. Electron. Mater., 2010, **39**, 1777–1781.

27   N. Wang, H. Chen, H. He, W. Norimatsu, M. Kusunoki and K. Koumoto, Sci. Rep., 2013, **3**, 3449.

28   S. P. Thompson, J. E. Parker, J. Potter, T. P. Hill, A. Birt, T. M. Cobb, F. Yuan and C. C. Tang, Rev. Sci. Instrum., 2009, **80**, 075107.

29   A. A. Coelho, J. Appl. Crystallogr., 2000, **33**, 899–908.

30   M. I. Mendelson, J. Am. Ceram. Soc., 1969, **52**, 443–446.

31   H. Muta, K. Kurosaki and S. Yamanaka, J. Alloys Compd., 2003, **350**, 292–295.

32   J. Okamoto, G. Shimizu, S. Kubo, Y. Yamada, H. Kitagawa, A. Matsushita, Y. Yamada and F. Ishikawa, J. Phys. Conf. Ser., 2009, **176**, 012042.

33   M. Mori, K. Nakamura and T. Itoh, J. Fuel Cell Sci. Technol., 2012, **9**, 021007.

34   A. I. Abutaha, S. R. S. Kumar, K. Li, A. M. Dehkordi, T. M. Tritt and H. N. Alshareef, Chem. Mater., 2015, **27**, 2165–2171.

35 N. Rezlescu and E. Rezlescu, *J. Am. Ceram. Soc.*, 1996, **79**, 2105–2108.

36 R. D. Shannon, *Acta Crystallogr.*, 1976, **A**, 751.

37 W. Gong, H. Yun, Y. B. Ning, J. E. Greedan, W. R. Datars and C. V. Stager, *J. Solid State Chem.*, 1991, **90**, 320–330.

38 F. Azough, S. S. Jackson, D. Ekren, R. Freer, M. Molinari, S. R. Yeandel, P. M. Panchmatia, S. C. Parker, D. H. Maldonado, D. M. Kepaptsoglou and Q. M. Ramasse, *ACS Appl. Mater. Interfaces*, 2017, **9**, 41988–42000.

39 L. Feng, T. Shiga and J. Shiomi, *Appl. Phys. Express*, 2015, **8**, 071501.

40 J. Mao, Y. Wang, Z. Liu, B. Ge and Z. Ren, *Nano Energy*, 2017, **32**, 174–179.

41 A. M. Glazer, *Acta Crystallogr. Sect. A*, 1975, **31**, 756–762.

42 D. I. Woodward and I. M. Reaney, *Acta Crystallogr. Sect. B Struct. Sci.*, 2005, **61**, 387–399.

43 L. Jones, H. Yang, T. J. Pennycook, M. S. J. Marshall, S. Van Aert, N. D. Browning, M. R. Castell and P. D. Nellist, *Adv. Struct. Chem. Imaging*, 2015, **1**, 8.

44 J. P. Buban, C. Miaofang, D. J. Masiel, J. P. Bradley, B. Jiang, H. Stahlberg and N. D. Browning, *J. Mater. Res.*, 2009, **24**, 2191–2199.

45 H. Du, C.-L. Jia, L. Houben, V. Metlenko, R. A. De Souza, R. Waser and J. Mayer, *Acta Mater.*, 2015, **89**, 344–351.

46 P. Gao, R. Ishikawa, B. Feng, A. Kumamoto, N. Shibata and Y. Ikuhara, *Ultramicroscopy*, 2018, **184**, 217–224.

47 D. Ferré, P. Carrez and P. Cordier, *Phys. Rev. B - Condens. Matter Mater. Phys.*, 2008, **77**, 1–7.

48 S. Y. Choi, S. D. Kim, M. Choi, H. S. Lee, J. Ryu, N. Shibata, T. Mizoguchi, E. Tochigi, T. Yamamoto, S. J. L. Kang and Y. Ikuhara, *Nano Lett.*, 2015, **15**, 4129–4134.

49 H. T. Kim, S. H. Kim, S. Nahm, J. D. Byun and Y. Kim, *J. Am. Ceram. Soc*, 1999, **82**, 3043–3048.

50 M. Hillert and G. R. Purdy, *Acta Metall.*, 1978, **26**, 333–340.

51 L. Chongmo and M. Hillert, *Acta Metall.*, 1981, **29**, 1949–1960.

52 H. E. Exner, *Met. Sci.*, 1982, **16**, 451–454.

53 V. V. Atuchin, T. A. Gavrilova, J. C. Grivel, V. G. Kesler and I. B. Troitskaia, *J. Solid State Chem.*, 2012, **195**, 125–131.

54 M. S. J. Marshall, D. T. Newell, D. J. Payne, R. G. Egdell and M. R. Castell, *Phys. Rev. B - Condens. Matter Mater. Phys.*, 2011, **83**, 1–6.

55 A. A. Yaremchenko, S. G. Patrício and J. R. Frade, *J. Power Sources*, 2014, **245**, 557–569.

56 M. Murata, K. Wakino and S. Ikeda, *J. Electron Spectros. Relat. Phenomena*, 1975, **6**, 459–464.

57 N. Aas, T. J. Pringle and M. Bowker, *J. Chem. Soc. Faraday Trans.*, 1994, **90**, 1015–1022.

58 R. Moos and K. H. Härdtl, *J. Appl. Phys.*, 1996, **80**, 393–400.

59 N. Wang, H. He, X. Li, L. Han and C. Zhang, *J. Alloys Compd.*, 2010, **506**, 293–296.

60   H. Taguchi, M. Sonoda and M. Nagao, J. Solid State Chem., 1998, **137**, 82–86.

61   S. Ohta, H. Ohta and K. Koumoto, J. Ceram. Soc. Japan, 2006, **114**, 102–105.

62   Y. F. Wang, K. H. Lee, H. Ohta and K. Koumoto, 2007 Int. Conf. Thermoelectr., 2008, **1**, 4–7.

63   S. Il Kim, K. H. Lee, H. A. Mun, H. S. Kim, S. W. Hwang, J. W. Roh, D. J. Yang, W. H. Shin, X. S. Li, Y. H. Lee, G. J. Snyder and S. W. Kim, Science (80-.)., 2015, **348**, 109–114.

64   H.-S. Kim, S. D. Kang, Y. Tang, R. Hanus and G. Jeffrey Snyder, Mater. Horiz., 2016, **3**, 234–240.

65   D. Kotchetkov, J. Zou, A. A. Balandin, D. I. Florescu and F. H. Pollak, Appl. Phys. Lett., 2001, **79**, 4316–4318.

66   R. L. Sproull, M. Moss and H. Weinstock, J. Appl. Phys., 1959, **30**, 334–337.

67   T. M. Tritt, Thermal conductivity Theory, Properties, and Applications, Kluwer Academic / Plenum Publishers, New York, 2004.

68   Z. Chen, B. Ge, W. Li, S. Lin, J. Shen, Y. Chang, R. Hanus, G. J. Snyder and Y. Pei, Nat. Commun., 2017, **8**, 1–8.

69   Z. Lu, H. Zhang, W. Lei, D. C. Sinclair and I. M. Reaney, Chem. Mater., 2016, **28**, 925–935.